Supporting Information for: **Projecting Global Mercury Emissions and Deposition Under the Shared Socioeconomic Pathways**

Benjamin M. Geyman[1], Colin P. Thackray[1], David G. Streets[1], Christine L. Olson[2], Kevin Schaefer[2], and Elsie M. Sunderland[1,3]

[1] Harvard John A. Paulson School of Engineering and Applied Sciences, Cambridge, MA 01238, USA.
[2] National Snow and Ice Data Center, Cooperative Institute for Research in Environmental Sciences, University of Colorado Boulder, Boulder, CO, USA
[3] Department of Environmental Health, Harvard School of Public Health, Boston, Massachusetts 02115, USA.

Contents of this file

Introduction

The supporting information contains 1 text section, 5 tables, and 5 figures.

Text S1. Global Biogeochemical Box Model Description

We simulate the temporal evolution of mercury in eleven global compartments using a modified version of the geochemical box model described in Amos et al. (2013). Model compartments include the atmosphere (ATM), three ocean compartments delineated based on depth (surface: OCS, intermediate: OCI, and deep: OCD), and three compartments for terrestrial vegetation and soils delineated based on organic carbon turnover time (fast: TF, slow: TS, and protected: TP).

We added four waste compartments to the existing model to track the fate of anthropogenic Hg emissions to land and water. Waste compartments are delineated based on turnover time in a manner analogous to terrestrial compartments, and are defined as fast (WF), slow (WS), protected (WP), and immobilized (WI). Model code is implemented in python and will be made available in a public repository upon publication.

Following Amos et al. (2013), the model is defined as a system of first-order differential equations:

$$\frac{\mathrm{dm}}{\mathrm{dt}} = \mathbf{K}\mathrm{m} + \mathrm{s}$$

In which *m* is a vector containing the mass in each of the seven reservoirs, *s* is a vector containing inputs to each reservoir and **K** is the 11 x 11 matrix of rate coefficients between each reservoir pair. We simulate the pre-anthropogenic natural steady state by solving dm/dt = 0 under a constant geogenic source of 230 Mg Hg a^{-1} to the atmosphere (Geyman et al., 2023) and 50 Mg a^{-1} to the deep ocean, reflecting the central estimate from Lamborg et al. (2006).

We construct **K** using values adapted from Amos et al. (2014). We updated the atmospheric budget for consistency with the most recent GEOS-Chem simulation from Shah et al. (2021). We adjusted setting fluxes associated with marine particles in the ocean based on more recent measurements of Hg partitioning to particles (Cui et al., 2021; Lamborg et al., 2016).

We force the model with historical anthropogenic emissions (1510-2010) from Streets et al. (2019) followed by projected future emissions under each SSP scenario. Cumulative historical emissions are 345 Gg Hg to the atmosphere, and 1127 Gg Hg to land and water. Land and water releases are categorized as mining (810 Gg) or non-mining (326 Gg). In each simulation year (*t*), the input vector, *s*(*t*), was updated to contain both geogenic sources and anthropogenic emissions.

Mining releases to land/water were allocated to terrestrial reservoirs, with 5% to the slow pool and 95% to the armored pool. All other releases followed the parameterization described in Streets et al. (2017) with 40% assumed to be sequestered and considered unavailable for active cycling. The remaining 60% was allocated among the new fast, slow and protected waste pools according to the relative carbon distribution in the analogous soil pools from the Global Terrestrial Mercury Model (Smith-Downey et al., 2010). Anthropogenic release magnitudes are linearly interpolated from the original decadal time resolution for use in the model.

Table S1. Present-day reservoirs and fluxes used to calculate first-order rate coefficients in 11-box model of Hg global biogeochemical cycling.

Atmosphere (ATM): 4.0 Gg[a]	**Flux (Mg a^{-1})**
Hg^{II} deposition to ocean	3900[a]
Hg^0 uptake by ocean, gross	2000[a]
Hg^{II} deposition to land	1600[a]
Hg^0 deposition to land	1200[a]
Surface Ocean (OCS): 2.9 Gg[b]	
Hg^0 gross evasion to the atmosphere	4800[a]
Hg^0 net evasion	2800[a]
Particle settling to intermediate ocean	3300[b]
Gross detrainment flux to intermediate ocean	5100[b]
Intermediate Ocean (OCI): 130 Gg[c]	
Particle settling to deep ocean	600
Upwelling intermediate to surface	7100[c]
Downwelling intermediate to deep	340[c]
Deep Ocean (OCD): 220 Gg[c]	
Particle settling; burial to deep sediment	210[c]
Upwelling deep to intermediate	180[c]
Fast Terrestrial (TF): 9.6 Gg[d]	
Evasion due to heterotrophic respiration of SOM	40[e]
Photoreduction	80[e]
Biomass burning; fast to atmosphere	290[f]
Riverine export to surface ocean	110[g]
Riverine export to continental margin sediment	600[g]
Decomposition; fast to slow	330[d]
Decomposition and mineral stabilization; fast to protected	10[d]
Slow Soil (TS): 35 Gg[d]	
Evasion due to heterotrophic respiration of SOM	20[e]
Biomass burning; slow to atmosphere	8[f]
Riverine export to surface ocean	3[g]
Riverine export to continental margin sediment	17[g]
Decomposition; slow to fast*	210[d]
Decomposition and mineral stabilization; slow to protected	0.5[d]
Protected Soil (TP): 190 Gg[d,**]	
Evasion due to heterotrophic respiration of SOM	3[e]
Biomass burning; protected to atmosphere	4[f]
Riverine export to surface ocean	2[g]
Riverine export to continental margin sediment	10[g]
Decomposition; protected to fast*	20[d]
External Inputs	
Subaerial volcanism emissions to atmosphere	230[h]
Submarine volcanism emissions to deep ocean	50[i]
Anthropogenic emissions to air, land, water	$f(t)$[j]

First-order rate coefficients, k, are calculated as $k_{ij} = F_{ij}/m_i$, where F_{ij} and m_i are the fluxes (Mg a^{-1}) and reservoir sizes (Gg) provided in the table above.

[a] Shah et al. (2021)

[b] Soerensen et al. (2010)

[c] Sunderland & Mason (2007)

[d] Smith-Downey et al. (2010)

[e] Amos et al. (2014). Values reflect downward revision of terrestrial evasion fluxes relative to Smith-Downey et al. (2010) based on observations and empirical models suggesting greater retention of deposited Hg than previous estimates (Hararuk et al., 2013; Obrist, 2012; Obrist et al., 2014).

[f] Total biomass burning is 300 Mg a^{-1} (Holmes et al., 2010) of which 95% is estimated to come from vegetation and 5% from the soil pools based on their carbon content (Smith-Downey et al., 2010).

[g] Based on present-day "background" global river discharge to terrestrial margin of 740 Mg a^{-1} from Amos et al. (2014), and assumption that 16% of riverine reaches open ocean based on estimate that all dissolved riverine Hg reaches the open ocean (9% of total) and 6-7% of particulate riverine Hg reaches the open ocean (Zhang et al., 2015). Riverine Hg not reaching the open

ocean is buried in continental margin sediment. Riverine Hg fluxes are sourced from terrestrial pools in the same manner as biomass burning, with 95% is estimated to come from vegetation and 5% from the soil pools based on their carbon content (Smith-Downey et al., 2010).

[h] Geyman et al. (2023)

[i] Lamborg et al., (2006)

[j] Function of time; see Methods in main text and Text S1 for more details.

* Transfer of soil Hg from longer-lived to shorter-lived reservoirs represents processes such as priming and changes in the degree of mineral stabilization of soil organic matter.

** Soil Hg reservoirs are based on global estimates made for organic soils using the Global Terrestrial Mercury Model (GTMM; Smith-Downey et al., 2010), a mechanistic global model facilitating self-consistent internal transfer and external Hg fluxes for the terrestrial biosphere. Large-scale geochemical soil survey results suggest greater total Hg mass in global topsoil than in the GTMM (Ballabio et al., 2021; Olson et al., 2022), but more work is needed to understand the implications of these findings for the terrestrial Hg budget.

105 **Table S2. Rate coefficients used in global biogeochemical box model.**

Compartment From (*i*)	Compartment To (*j*)	Rate (a^{-1})*
Atmosphere	Terrestrial Fast	5.00×10^{-1}
	Terrestrial Slow	1.28×10^{-1}
	Terrestrial Protected	7.20×10^{-2}
	Ocean Surface	1.47×10^{0}
Terrestrial Fast	Atmosphere	4.36×10^{-2}
	Terrestrial Slow	3.44×10^{-2}
	Terrestrial Protected	1.04×10^{-3}
	Ocean Surface	1.24×10^{-2}
	Margin Sediment Burial	6.16×10^{-2}
Terrestrial Slow	Atmosphere	9.43×10^{-4}
	Terrestrial Fast	6.00×10^{-3}
	Terrestrial Protected	1.43×10^{-5}
	Ocean Surface	8.97×10^{-5}
	Margin Sediment Burial	4.45×10^{-4}
Terrestrial Protected	Atmosphere	3.68×10^{-5}
	Terrestrial Fast	7.89×10^{-5}
	Ocean Surface	9.01×10^{-6}
	Margin Sediment Burial	4.47×10^{-5}
Ocean Surface	Atmosphere	1.66×10^{0}
	Ocean Intermediate	2.90×10^{0}
Ocean Intermediate	Ocean Surface	5.46×10^{-2}
	Ocean Deep	7.23×10^{-3}
Ocean Deep	Ocean Intermediate	8.18×10^{-4}
	Marine Sediment Burial	9.55×10^{-4}
Waste Fast	Atmosphere	4.36×10^{-2}
	Terrestrial Slow	3.44×10^{-2}
	Terrestrial Protected	1.04×10^{-3}
	Ocean Surface	1.24×10^{-2}
	Margin Sediment Burial	6.16×10^{-2}
Waste Slow	Atmosphere	9.43×10^{-4}
	Terrestrial Fast	6.00×10^{-3}
	Terrestrial Protected	1.43×10^{-5}
	Ocean Surface	8.97×10^{-5}
	Margin Sediment Burial	4.45×10^{-4}
Waste Protected	Atmosphere	3.68×10^{-5}
	Terrestrial Fast	7.89×10^{-5}
	Ocean Surface	9.01×10^{-6}
	Margin Sediment Burial	4.47×10^{-5}

Compartment From (*i*)	**Compartment To** (*j*)	**Rate** (a^{-1})*
Waste Immobile	Atmosphere	1.00×10^{-20}

*Rates are calculated from the sum of fluxes in cases where mass transfer between a pair of reservoirs (*i,j*) is composed of multiple fluxes.

Table S3. Global Biogeochemical Box Model Evaluation

Constraint Description	Model Value	Reference Value
Mass Hg in modern troposphere (Gg)	3.9	4.0[a]
Upper ocean Hg concentration (0-1500 m) (pM)	1.2	0.8 – 1.8[b]
Deep ocean (>1500m) Hg concentration (pM)	1.2	1.1 – 1.7[b]
Pre-industrial to modern atmospheric Hg deposition enrichment factor (1840-20th century maximum)	4.1	3 – 5[c]

[a] Shah et al. (2021)

[b] (Lamborg et al., 2014; Sunderland & Mason, 2007)

[c] (Fitzgerald et al., 2005; Li et al., 2020; Sonke et al., 2023)

Table S4. Mercury emissions by region for the base year and key future years (Mg a^{-1})

1-2.6	2010	2030	2050	2100	2150	2200	2250
NAM	109.3	79.4	44.8	12.8	8.8		
SAM	263.6	253.9	153.4	9.8	6.7		
EUR	85.7	30.7	16.7	7.0	4.8		
FSU	86.5	107.7	53.9	9.3	6.4		
AFM	383.2	363.4	251.1	21.1	14.5		
ASA	1255.5	1115.3	597.8	90.9	62.6		
OCA	25.6	15.3	8.3	3.5	2.4		
GLO	2209.4	1965.8	1126.0	154.3	106.3	0	0
2-4.5	2010	2030	2050	2100	2150	2200	2250
NAM	109.3	92.2	61.4	15.8	10.5	5.3	
SAM	263.6	261.0	159.9	13.4	8.9	4.5	
EUR	85.7	37.9	26.2	8.6	5.7	2.9	
FSU	86.5	124.2	74.8	11.1	7.4	3.7	
AFM	383.2	388.1	293.7	34.4	23.0	11.5	
ASA	1255.5	1325.3	841.0	104.9	69.9	35.0	
OCA	25.6	18.9	13.1	4.3	2.9	1.4	
GLO	2209.4	2247.7	1470.2	192.5	128.3	64.2	0
5-3.4	2010	2030	2050	2100	2150	2200	2250
NAM	109.3	99.8	44.7	9.5	6.3		
SAM	263.6	270.7	155.6	7.4	4.9		
EUR	85.7	41.8	16.5	5.2	3.5		
FSU	86.5	123.1	52.7	5.4	3.6		
AFM	383.2	452.0	278.3	17.3	11.5		
ASA	1255.5	1568.6	678.0	59.0	39.1		
OCA	25.6	20.9	8.2	2.6	1.7		
GLO	2209.4	2576.9	1234.0	106.6	70.6	0	0
5-8.5	2010	2030	2050	2100	2150	2200	2250
NAM	109.3	81.4	82.5	38.5	21.5	10.8	
SAM	263.6	264.7	184.7	31.4	17.6	8.8	
EUR	85.7	31.2	37.2	21.0	11.8	5.9	
FSU	86.5	80.9	103.7	33.4	18.7	9.3	
AFM	383.2	428.7	527.9	422.9	236.9	118.4	
ASA	1255.5	1198.8	1155.8	356.7	199.8	99.9	
OCA	25.6	15.6	18.6	10.5	5.9	2.9	
GLO	2209.4	2101.2	2110.3	914.3	512.1	256.1	0

Region names: NAM = North America, SAM = South America, EUR = Western Europe, FSU = Former Soviet Union, AFM = Africa and the Middle East, ASA = Asia, OCA = Oceania.

117 **Table S5. Mercury emissions by source category for the base year and key future years (Mg a^{-1})**

1-2.6	2010	2030	2050	2100	2150	2200	2250
Mining and Industry	491.1	556.9	445.3	121.5	83.7		
Artisanal Gold Mining	726.8	726.8	457.3	0	0		
Coal Combustion	538.2	375.2	79.6	5.1	3.5		
Oil Combustion	14.5	17.1	13.0	3.7	2.5		
Other	438.9	289.8	130.8	24.1	16.6		
Total	2209.4	1965.8	1126.0	154.3	106.3	0	0
2-4.5	2010	2030	2050	2100	2150	2200	2250
Mining and Industry	491.1	556.9	445.3	121.5	81.0	40.5	
Artisanal Gold Mining	726.8	726.8	457.3	0	0	0	
Coal Combustion	538.2	584.7	372.0	10.9	7.3	3.6	
Oil Combustion	14.5	20.9	23.9	16.9	11.2	5.6	
Other	438.9	358.4	171.7	43.3	28.9	14.4	
Total	2209.4	2247.7	1470.2	192.5	128.3	64.2	0
5-3.4	2010	2030	2050	2100	2150	2200	2250
Mining and Industry	491.1	565.3	443.4	85.6	56.7		
Artisanal Gold Mining	726.8	726.8	457.3	0	0		
Coal Combustion	538.2	888.4	187.8	0.8	0.5		
Oil Combustion	14.5	18.4	22.7	7.4	4.9		
Other	438.9	378.0	122.8	12.8	8.5		
Total	2209.4	2576.9	1234.0	106.6	70.6	0	0
5-8.5	2010	2030	2050	2100	2150	2200	2250
Mining and Industry	491.1	565.3	443.4	85.6	48.0	24.0	
Artisanal Gold Mining	726.8	726.8	457.3	0	0	0	
Coal Combustion	538.2	539.6	985.8	775.3	434.2	217.1	
Oil Combustion	14.5	28.5	32.7	15.2	8.5	4.2	
Other	438.9	241.0	191.1	38.3	21.5	10.7	
Total	2209.4	2101.2	2110.3	914.3	512.1	256.1	0

118

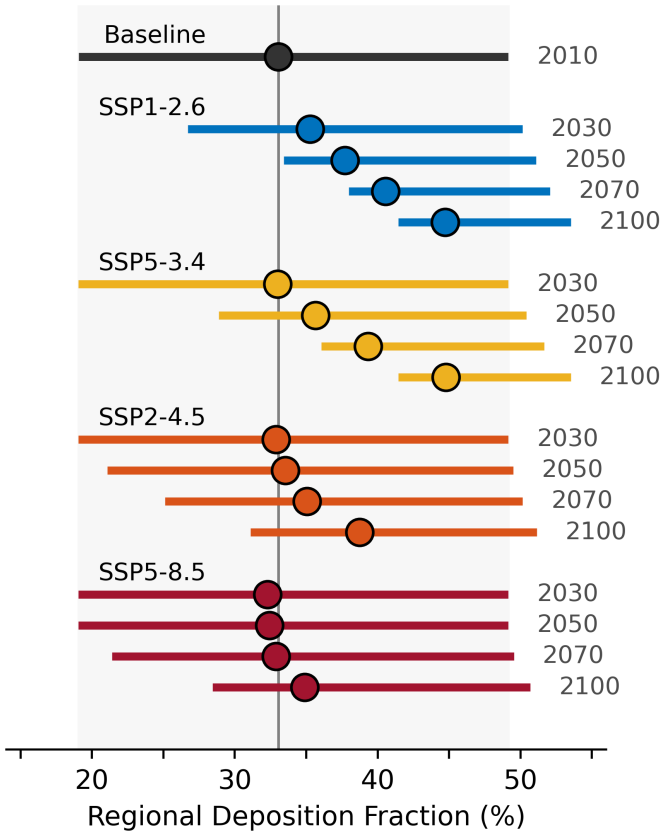

Figure S1. Trends in the fraction of anthropogenic emissions redepositing to region of origin. Lines represent the range among individual world regions and points represent the fraction of total anthropogenic emissions that re-deposit to the region of origin. Values are separated by scenario (SSP1-2.6, SSP5-3.4, SSP2-4.5, SSP5-8.5) and presented for selected years (2030, 2050, 2070, 2100). Values for the baseline year (2010) are shown at the top of the figure in black, with the central value (vertical grey line) and regional range (grey shaded area) shown for comparison. Trends are driven by changes in the speciation of anthropogenic emissions. As the percentage of total Hg released as elemental Hg (Hg^0) declines in anthropogenic Hg emissions to air, the fraction of anthropogenic emissions redepositing to the region of origin increases. Note that the speciation of anthropogenic emissions continues to shift towards lower Hg^0 percentages beyond 2100 (Fig. 2).

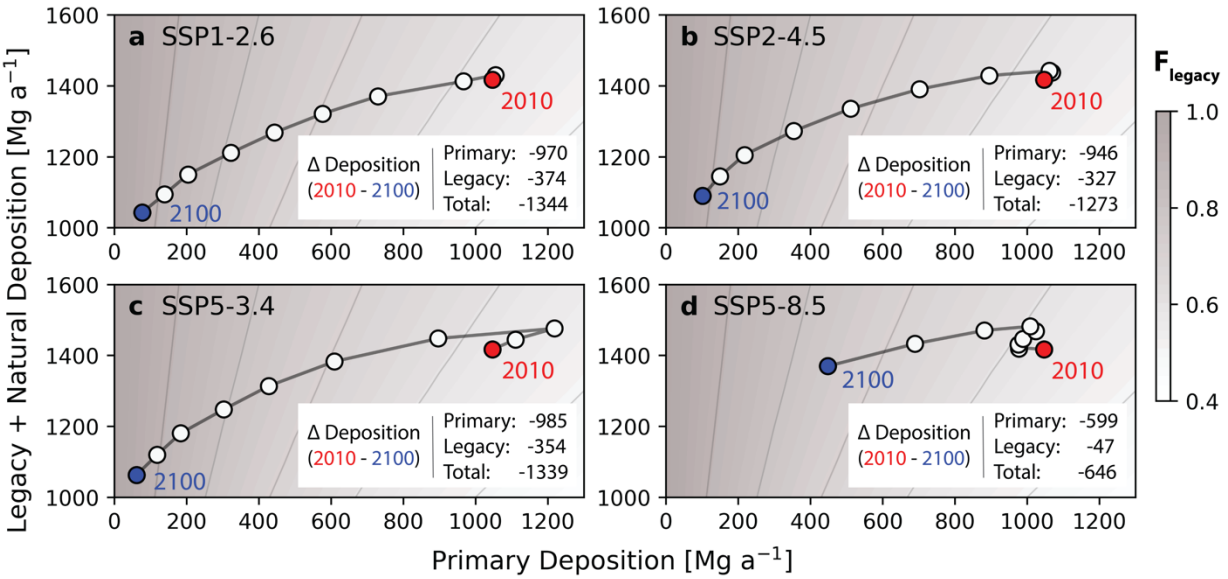

Figure S2. Trajectories of atmospheric mercury (Hg) deposition from primary anthropogenic and legacy + natural emissions. Changes in the emission drivers of deposition can be visualized over sequential decadal snapshots from 2010 (blue) to 2100 (red). Deposition is calculated over ice-free land surfaces, with total deposition being the sum of deposition from legacy + natural emissions (y-axis) and deposition from primary anthropogenic emissions (x-axis). Panels **a – d** represent different Shared Socioeconomic Pathway (SSP) scenarios. The background of each panel is shaded to show the fraction of total deposition from legacy + natural sources. Inset annotations indicate the change in deposition between 2010 and 2100 for each category. Note that all temporal change in the "legacy + natural" deposition category is due to change in the legacy component because natural deposition is fixed.

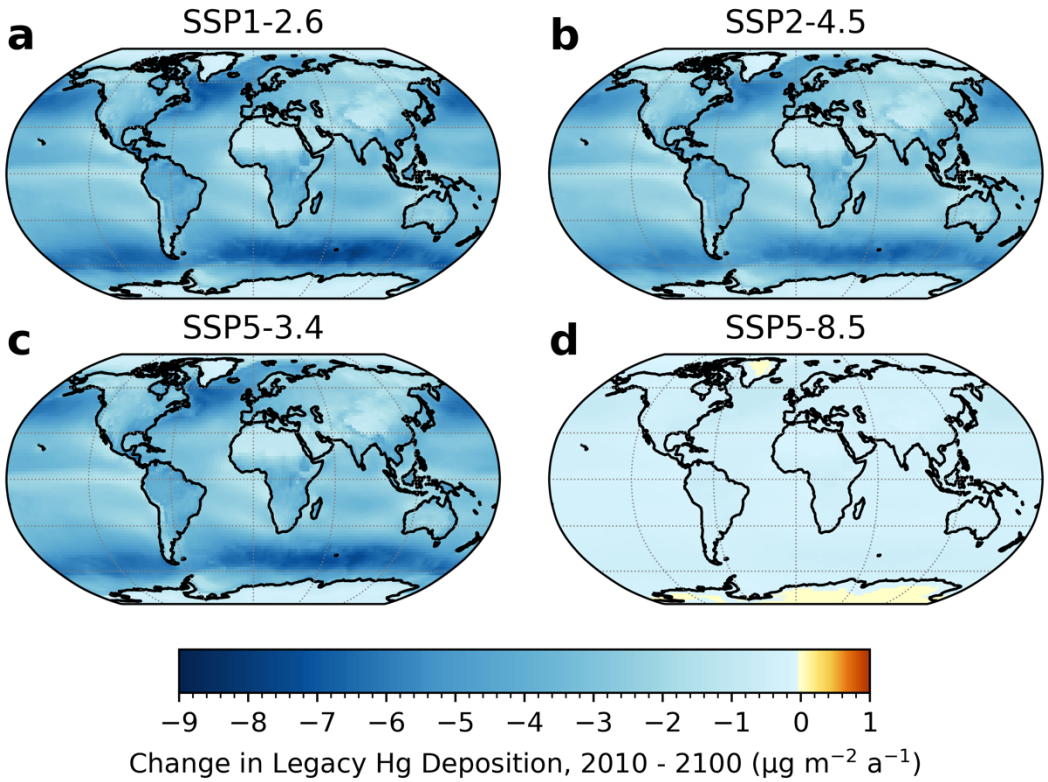

Figure S3. Change in atmospheric mercury (Hg) deposition from legacy emissions, 2010-2100. Patterns of deposition for 2010 and 2100 are calculated based on emissions from the ocean and terrestrial biosphere, which are quantified by forcing the global biogeochemical box model (GBBM) with historical (1510-2010) emissions from Streets et al. (2019) and scenario-specific future emissions. Emissions from the ocean and terrestrial biosphere include a "natural" component, though all change in the deposition shown here is attributable to change in legacy emissions because natural emissions are fixed. Deposition change is calculated as the difference between 2100 and 2010 values.

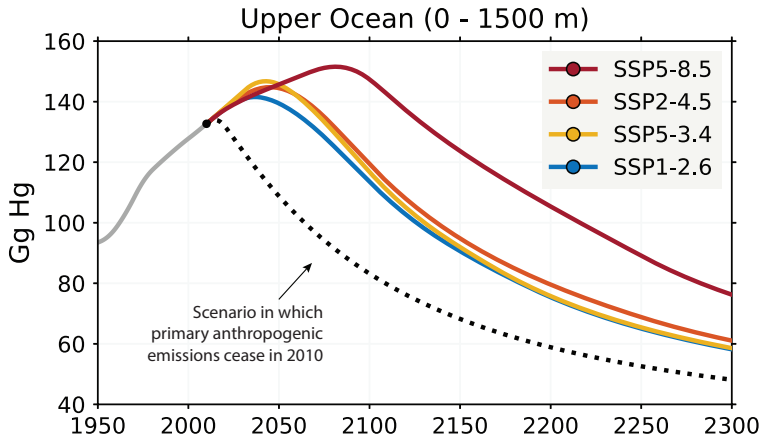

Figure S4. Scenario-specific mass trajectories of mercury (Hg) in the upper ocean (0-1500 m). Trajectories under future emissions (2010-2300) are shown for SSPs 1-2.6 (blue), 2-4.5 (orange), 5-3.4 (yellow), and 5-8.5 (red), in addition to a reference scenario in which primary anthropogenic emissions cease in 2010 (dashed black).

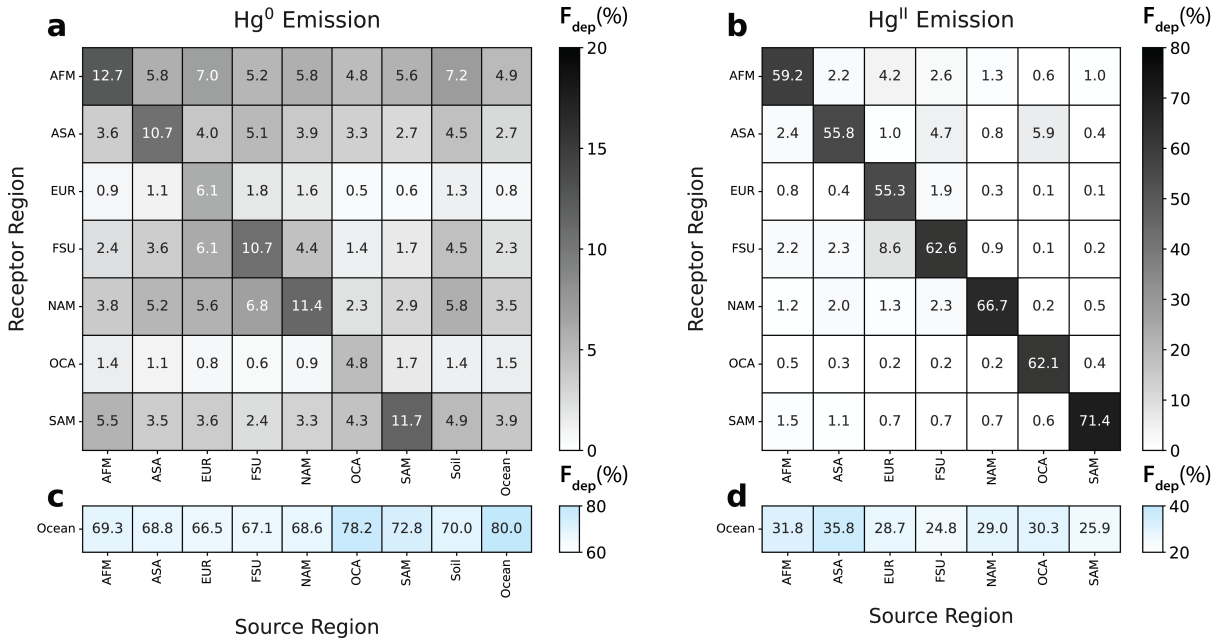

Figure S5. Mercury source-receptor matrices, by species. Matrix elements represent the fraction of a unit emission from a given source (column) to a given receptor (row). Source-receptor matrices are presented for emissions of gaseous elemental mercury (panels **a** and **c**) and gaseous oxidized mercury (panels **b** and **d**). Note that the sum down an entire column in (**a**, **c**) and (**b**, **d**) is close to, but not quite 1, resulting from a small fraction of deposition which occurs to global ice surfaces and a rapid re-emission process in the model. Also note the differences in color scale between species.

References

Amos, H. M., Jacob, D. J., Streets, D. G., & Sunderland, E. M. (2013). Legacy impacts of all-time anthropogenic emissions on the global mercury cycle. *Global Biogeochemical Cycles*, *27*(2), 410–421. https://doi.org/10.1002/gbc.20040

Amos, H. M., Jacob, D. J., Kocman, D., Horowitz, H. M., Zhang, Y., Dutkiewicz, S., et al. (2014). Global Biogeochemical Implications of Mercury Discharges from Rivers and Sediment Burial. *Environmental Science & Technology*, *48*(16), 9514–9522. https://doi.org/10.1021/es502134t

Ballabio, C., Jiskra, M., Osterwalder, S., Borrelli, P., Montanarella, L., & Panagos, P. (2021). A spatial assessment of mercury content in the European Union topsoil. *Science of the Total Environment*, *769*, 144755. https://doi.org/10.1016/j.scitotenv.2020.144755

Cui, X., Lamborg, C. H., Hammerschmidt, C. R., Xiang, Y., & Lam, P. J. (2021). The Effect of Particle Composition and Concentration on the Partitioning Coefficient for Mercury in Three Ocean Basins. *Frontiers in Environmental Chemistry*, *2*(May), 1–16. https://doi.org/10.3389/fenvc.2021.660267

Fitzgerald, W. F., Engstrom, D. R., Lamborg, C. H., Tseng, C. M., Balcom, P. H., & Hammerschmidt, C. R. (2005). Modern and historic atmospheric mercury fluxes in northern Alaska: Global sources and arctic depletion. *Environmental Science and Technology*, *39*(2), 557–568. https://doi.org/10.1021/es049128x

Geyman, B. M., Thackray, C. P., Jacob, D. J., & Sunderland, E. M. (2023). Impacts of Volcanic Emissions on the Global Biogeochemical Mercury Cycle: Insights from Satellite Observations and Chemical Transport Modeling. *Geophysical Research Letters*, *50*, e2023GRL104667. https://doi.org/10.1029/2023GL104667

Hararuk, O., Obrist, D., & Luo, Y. (2013). Modelling the sensitivity of soil mercury storage to climate-induced changes in soil carbon pools. *Biogeosciences*, *10*(4), 2393–2407. https://doi.org/10.5194/bg-10-2393-2013

Holmes, C. D., Jacob, D. J., Corbitt, E. S., Mao, J., Yang, X., Talbot, R., & Slemr, F. (2010). Global atmospheric model for mercury including oxidation by bromine atoms. *Atmospheric Chemistry and Physics*, *10*(24), 12037–12057. https://doi.org/10.5194/acp-10-12037-2010

Lamborg, C. H., Von Damm, K. L., Fitzgerald, W. F., Hammerschmidt, C. R., & Zierenberg, R. (2006). Mercury and monomethylmercury in fluids from Sea Cliff submarine hydrothermal field, Gorda Ridge. *Geophysical Research Letters*, *33*(17), L17606. https://doi.org/10.1029/2006GL026321

Lamborg, C. H., Hammerschmidt, C. R., Bowman, K. L., Swarr, G. J., Munson, K. M., Ohnemus, D. C., et al. (2014). A global ocean inventory of anthropogenic mercury based on water column measurements. *Nature*, *512*(7512), 65–68. https://doi.org/10.1038/nature13563

Lamborg, C. H., Hammerschmidt, C. R., & Bowman, K. L. (2016). An examination of the role of particles in oceanic mercury cycling. *Philosophical Transactions of the Royal Society A: Mathematical, Physical and Engineering Sciences*, *374*(2081). https://doi.org/10.1098/rsta.2015.0297

Li, C., Sonke, J. E., Le Roux, G., Piotrowska, N., Van der Putten, N., Roberts, S. J., et al. (2020). Unequal Anthropogenic Enrichment of Mercury in Earth's Northern and Southern Hemispheres. *ACS Earth and Space Chemistry*, *4*(11), 2073–2081. https://doi.org/10.1021/acsearthspacechem.0c00220

Obrist, D. (2012). Mercury Distribution across 14 U.S. Forests. Part II: Patterns of Methyl Mercury Concentrations and Areal Mass of Total and Methyl Mercury. *Environmental Science & Technology*, *46*(11), 5921–5930. https://doi.org/10.1021/es2045579

Obrist, D., Pokharel, A. K., & Moore, C. (2014). Vertical Profile Measurements of Soil Air Suggest Immobilization of Gaseous Elemental Mercury in Mineral Soil. *Environmental Science & Technology*, *48*(4), 2242–2252. https://doi.org/10.1021/es4048297

Olson, C. I., Geyman, B. M., Thackray, C. P., Krabbenhoft, D. P., Tate, M. T., Sunderland, E. M., & Driscoll, C. T. (2022). Mercury in soils of the conterminous United States: patterns and pools. *Environmental Research Letters*, *17*(7), 074030. https://doi.org/10.1088/1748-9326/ac79c2

Shah, V., Jacob, D. J., Thackray, C. P., Wang, X., Sunderland, E. M., Dibble, T. S., et al. (2021). Improved Mechanistic Model of the Atmospheric Redox Chemistry of Mercury. *Environmental Science & Technology*, acs.est.1c03160. https://doi.org/10.1021/acs.est.1c03160

Smith-Downey, N. V., Sunderland, E. M., & Jacob, D. J. (2010). Anthropogenic impacts on global storage and emissions of mercury from terrestrial soils: Insights from a new global model. *Journal of Geophysical Research*, *115*(G3), G03008. https://doi.org/10.1029/2009JG001124

Soerensen, A. L., Sunderland, E. M., Holmes, C. D., Jacob, D. J., Yantosca, R. M., Skov, H., et al. (2010). An Improved Global Model for Air-Sea Exchange of Mercury: High Concentrations over the North Atlantic. *Environmental Science & Technology*, *44*(22), 8574–8580. https://doi.org/10.1021/es102032g

Sonke, J. E., Angot, H., Zhang, Y., Poulain, A., Björn, E., & Schartup, A. (2023). Global change effects on biogeochemical mercury cycling. *Ambio*, *52*(5), 853–876. https://doi.org/10.1007/s13280-023-01855-y

Streets, D. G., Horowitz, H. M., Jacob, D. J., Lu, Z., Levin, L., ter Schure, A. F. H., & Sunderland, E. M. (2017). Total Mercury Released to the Environment by Human Activities. *Environmental Science & Technology*, *51*(11), 5969–5977. https://doi.org/10.1021/acs.est.7b00451

Streets, D. G., Horowitz, H. M., Lu, Z., Levin, L., Thackray, C. P., & Sunderland, E. M. (2019). Five hundred years of anthropogenic mercury: spatial and temporal release profiles*. *Environmental Research Letters*, *14*(8), 084004. https://doi.org/10.1088/1748-9326/ab281f

Sunderland, E. M., & Mason, R. P. (2007). Human impacts on open ocean mercury concentrations. *Global Biogeochemical Cycles*, *21*(4). https://doi.org/10.1029/2006GB002876

Zhang, Y., Jacob, D. J., Dutkiewicz, S., Amos, H. M., Long, M. S., & Sunderland, E. M. (2015). Biogeochemical drivers of the fate of riverine mercury discharged to the global and Arctic oceans. *Global Biogeochemical Cycles*, *29*(6), 854–864. https://doi.org/10.1002/2015GB005124